پژوهش‌های باستان‌شناسی ایران 49

Bu-Ali Sin University
Iranian Scientific Archaeological Association

پژوهش‌های باستان‌شناسی ایران
Archaeological Research of Iran
P. ISSN: 2345-5225 & E. ISSN: 2345-5500
Homepage: https://nbsh.basu.ac.ir/
Vol. 16, No. 49, 2026

Manufacturing Technology and Corrosion Mechanisms of Ancient Metal Artifacts from Qalaichi Tepe

Hamidreza Bakhshandehfard[1], Zahra Rahimi Kelishadi[2], Farshid Iravani Ghadim[3]

https://doi.org/10.22084/nb.2025.9515.2664
Received: 2024/04/05; Revised: 2024/07/17; Accepted: 2024/07/29
Type of Article: **Research**
Pp: 147-181

Abstract

The Mannaean Kingdom was one of the major Iron Age polities that flourished in northwestern Iran during the first millennium BCE. Qalaichi Tepe, identified as the Mannaean capital Izirtu, represents one of the most significant archaeological sites of this period. This study investigates nine copper-based artifacts recovered from systematic excavations conducted at Qalaichi between 2002 and 2004 under the direction of Bahman Karegar. The assemblage comprises a complete bracelet, one fragmented object, and seven additional metal fragments dating to the first millennium BCE. The research aims to reconstruct manufacturing technology, characterize microstructural features, identify corrosion products, and assess the corrosion mechanisms affecting these artifacts. To achieve these objectives, optical microscopy, metallography, scanning electron microscopy coupled with energy-dispersive X-ray spectroscopy (SEM–EDS), and X-ray diffraction (XRD) were employed. Microstructural observations indicate that the artifacts were manufactured through combinations of casting, cold working, hot working, and repeated annealing, reflecting advanced metallurgical knowledge. SEM–EDS analyses showed that seven artifacts were made of tin bronze, whereas two specimens consisted of nearly pure copper. Elongated sulfide inclusions preserved within the metallic matrix indicate incomplete smelting of sulfidic copper ores and provide evidence for the nature of raw materials and extraction technology. XRD identified the principal corrosion products as cuprite (Cu_2O), nantokite ($CuCl$), malachite ($Cu_2CO_3(OH)_2$), and brochantite ($Cu_4SO_4(OH)_6$), reflecting complex burial-induced corrosion processes. Microstructural evidence further demonstrates selective corrosion characterized by preferential dissolution of the copper-rich phase, secondary tin enrichment, intergranular corrosion, microcracking, and localized porosity. Despite variations in corrosion intensity, the artifacts exhibit notably similar manufacturing characteristics, suggesting standardized metallurgical practices within Mannaean workshops. These findings provide new insights into Iron Age copper-alloy production technology in northwestern Iran while contributing valuable archaeometallurgical data for understanding Mannaean metallurgy and informing the conservation of archaeological copper-based cultural heritage.

Keywords: Qalaichi Tepe, Mannaean Culture, Manufacturing Technology, Corrosion Mechanisms, SEM–EDS.

1. Department of Conservation and Restoration of Cultural and Historical Objects, Faculty of Conservation and Restoration Art University of Isfahan, Isfahan, Iran (Corresponding Author).
Email: hr.bakhshan@aui.ac.ir
2. Department of Conservation and Restoration of Cultural and Historical Objects, Faculty of Conservation and Restoration Art University of Isfahan, Isfahan, Iran.
3. Department of Archaeology, Faculty of Cultural Materials Conservation, Tabriz Islamic Art University, Tabriz, Iran.

Citations: Bakhshandefard, H., Rahimi Kelishadi, Z. & Iravan Ghadim, F., (2026). "Manufacturing Technology and Corrosion Mechanisms of Ancient Metal Artifacts from Qalaichi Tepe". *Archaeological Research of Iran,* 16(49): 147-181. https://doi.org/10.22084/nb.2025.9515.2664

Journal of Department of Archaeology, Faculty of Art and Architecture, Bu-Ali Sina University, Hamadan, Iran.

Copyright © 2026 The Authors. Published by Bu-Ali Sina University.
This work is licensed under a Creative Commons Attribution-NonCommercial 4.0 International license (https://creativecommons.org/licenses/by-nc/4.0/). Non-commercial uses of the work are permitted, provided the original work is properly cited.

© The Author(s)

Introduction

The Mannaean Kingdom was one of the most prominent civilizations of northwestern Iran during the first millennium BCE. Prior to the emergence of the Median Kingdom, several local polities had developed across western and northwestern Iran, among which the Mannaean Kingdom distinguished itself through its political authority, territorial extent, cultural achievements, and historical significance. Established during the first millennium BCE, the kingdom endured for more than three centuries. According to Assyrian textual sources, Manna was governed under a monarchical political system. Several important archaeological sites associated with the Mannaean cultural horizon have been excavated, including Qalaichi, Ziwiyeh, Zendan-e Soleyman, Kul Tarikeh, and Hasanlu. Qalaichi Tepe is located approximately 8 km northeast of the city of Bukan in West Azerbaijan Province, Iran. Archaeological evidence indicates that the site represents a Mannaean occupation layer dating to approximately the eighth and seventh centuries BCE (ca. 800–600 BCE). Based on the Aramaic inscription discovered at the site, Qalaichi has been identified as Izirtu (also rendered as Zirtu), the capital of the Mannaean Kingdom (Molazadeh, 2009: 45–53). Despite extensive looting and the illicit removal of numerous archaeological objects, the remaining artifacts recovered from Qalaichi continue to demonstrate the exceptional archaeological significance of the site, while archaeological evidence strongly supports its identification as the Mannaean capital. Following widespread illegal excavations, a rescue excavation was undertaken in 1985 under the direction of Ehsan Yaghmaei (Yaghmaei, 2023). Archaeological investigations subsequently ceased for several years before systematic excavations resumed in 1999 under the direction of Bahman Karegar and continued until 2006. However, the results of these excavations have been reported only in a brief publication (Karegar, 2004: 229–245). Excavations at Qalaichi uncovered an extensive architectural complex comprising a monumental entrance gateway, a stone-paved courtyard, a columned hall, a series of adjoining rooms, and several raised platforms. The buildings were constructed on stone rubble foundations bonded with mud mortar and featured large mudbrick walls comparable in architectural style to those identified at Ziwiyeh. These architectural remains, together with the rich assemblage of archaeological materials recovered from the site, provide valuable evidence for understanding the political organization, architectural traditions, and material culture of the Mannaean Kingdom during the Iron Age.

Research Aims and Significance: The artifacts examined in this study were recovered from Qalaichi Tepe during archaeological excavations conducted between 2002 and 2004 under the direction of Bahman Karegar. Dating to the first millennium BCE, the assemblage comprises two principal groups. The first group consists of an intact bronze bracelet and a fragment of a broken bronze object, whereas the second comprises seven metal artifacts that vary in morphology, dimensions, degree of corrosion, and alloy composition. Collectively, these objects are likely to represent a range of functions within Mannaean society, including ornamental, utilitarian, and possibly ritual purposes.

The primary objective of this study is to characterize these artifacts through archaeometallurgical investigation by identifying their manufacturing technology, alloy composition, and corrosion products. Owing to their geographical provenance and chronological attribution to the first millennium BCE, these artifacts constitute an important source of evidence for reconstructing the technological, cultural, and socioeconomic development of Iron Age communities in northwestern Iran. The significance of this research lies in two complementary aspects: first, the investigation of ancient metallurgical technology, including manufacturing techniques and alloy composition; and second, the characterization of corrosion processes and structural alterations resulting from long-term burial and post-depositional environmental conditions. Determining the chemical composition and manufacturing technology of these artifacts provides valuable insights into the technological capabilities, availability of raw materials, and metallurgical traditions of the Mannaean Kingdom. For example, variations in the tin-to-copper ratio of bronze alloys may reflect the extent to which ancient craftsmen intentionally controlled the mechanical properties of their products. Likewise, the identification of minor and trace alloying or impurity elements, such as arsenic, lead, iron, and nickel, can contribute to provenance studies, the reconstruction of ancient exchange networks, and the assessment of technological interactions between the Mannaeans and neighboring cultures, including Urartu, Assyria, and the Caucasian communities. From a conservation perspective, investigating corrosion mechanisms and deterioration processes not only improves our understanding of burial environments and post-depositional alteration but also provides essential information for developing appropriate conservation and preservation strategies. Mineralogical characterization of corrosion products including malachite, cuprite, and tenorite using X-ray diffraction (XRD) and scanning electron microscopy coupled with energy-

dispersive X-ray spectroscopy (SEM–EDS) enables accurate identification of corrosion phases and their stability, thereby providing insights into the long-term degradation behavior of copper-based alloys in the burial soils of the region. Beyond the characterization of individual artifacts, studies of this nature contribute to a broader understanding of the role of metallurgy within the economic, technological, and cultural framework of the Mannaean Kingdom and the evolution of metalworking traditions in northwestern Iran. Given the scarcity of written historical sources for the Mannaean period, archaeometallurgical evidence derived from material culture represents an indispensable source of information for reconstructing the technological history of this Iron Age civilization.

Research Questions: This study investigates nine archaeological metal artifacts recovered from Qalaichi Tepe through an integrated archeometallurgical and conservation-based approach to elucidate their manufacturing technology and deterioration processes. The research addresses the following questions: 1) What manufacturing techniques were employed in the production of these artifacts, as inferred from their microstructural and metallurgical characteristics? 2) What are the principal corrosion products present in the artifacts, and what is their degree of stability? 3) What corrosion mechanisms and environmental factors have governed the deterioration of these archaeological objects during burial?

Literature Review

Archaeological and historical investigations of the Mannaean Kingdom and its associated sites in northwestern Iran have attracted considerable scholarly attention since the 1960s. Among the earliest contributions, Dyson (1965) conducted extensive archaeological investigations at major sites such as Hasanlu and Ziwiyeh, publishing a series of studies on their cultural sequence, archaeological context, and material remains (Dyson, 1965: 193–217). Subsequently, Muscarella (1988: 105–109) provided a comprehensive overview of Urartian sites and the archaeological landscape of northwestern Iran, thereby placing the Mannaean cultural sphere within a broader regional context. Iranian scholars have likewise made significant contributions to the study of the Mannaean Kingdom. Behzadi (1993) examined its political organization, socioeconomic structure, relationships with neighboring states, as well as its language, religion, artistic traditions, and selected archaeological finds. Hassanzadeh (2006) investigated the architectural remains of Mannaean sites while also discussing the kingdom's political history, administrative organization,

language, script, and artistic achievements. Malekzadeh (2009) focused on the emergence of the Medes and the Mannaeans in northwestern Iran, emphasizing the historical geography and political development of the region. Similarly, Mollazadeh (2009) identified the Mannaean Kingdom as one of the earliest political entities in western and northwestern Iran and provided a comprehensive assessment of its cultural history, ethnicity, language, writing system, political organization, economy, and provincial administration. In this study, Qalaichi was identified as Izirtu, the capital of the Mannaean Kingdom. Further archaeological investigations have expanded knowledge of the Mannaean cultural landscape. Qodratabadi & Co-workers (2009) examined the Qaplantu archaeological site, describing its geographical setting, archaeological context, chronological sequence, and excavated artifacts. Another significant discovery is the Bukan Stele, unearthed during excavations between 1999 and 2004, whose Aramaic inscription explicitly identifies Qalaichi as the capital of the Mannaean Kingdom. Despite these substantial archaeological and historical investigations, archaeometallurgical research on Mannaean metal artifacts, particularly material from Qalaichi, remains notably limited. To date, no comprehensive study has specifically examined the manufacturing technologies and corrosion characteristics of copper-based artifacts from this site. Several technical studies have nevertheless examined archaeological metals recovered in the Bukan region. Bahadari & Ahmadi (2000) conducted laboratory analyses of corrosion phenomena in excavated iron artifacts using microscopy and phase-identification techniques. Their study identified corrosion phases including goethite, lepidocrocite, and magnetite, and demonstrated the substantial influence of soil composition, moisture, and acidic environmental conditions on the progressive deterioration of archaeological iron (Bahadari & Ahmadi, 2000: 117–125). Soudagar (1995) investigated the technological characteristics of metal artifacts from Bukan, focusing on alloy composition, production techniques, manufacturing processes, and decorative practices. The study emphasized the importance of interdisciplinary archaeometallurgical approaches for understanding ancient metalworking traditions. Likewise & Bahadari (1998) examined the structural characteristics and deterioration patterns of several iron objects excavated from Qalaichi (Bahadari, 1998). Their research documented layered, exfoliative, and intergranular forms of corrosion and highlighted the role of chloride- and sulfide-bearing burial environments in accelerating deterioration. The authors further proposed conservation strategies for stabilizing these archaeological metals. More

recently, Hassanzadeh (2022) produced one of the most comprehensive archaeological syntheses of the Mannaean Kingdom. Drawing on archaeological excavations and regional surveys undertaken over the past five decades, the study reconstructs Mannaean material culture from archaeological evidence rather than relying primarily on Assyrian and Urartian textual sources. Hassanzadeh identifies a set of diagnostic archaeological indicators for recognizing Mannaean sites, including columned halls, raised floors, stone foundations, decorated mudbrick architecture, glazed or ochre-colored bricks, glazed pottery, and ivory artifacts. Although not all these characteristics occur at every site, their co-occurrence provides a reliable framework for identifying Mannaean settlements. The study further highlights the geopolitical significance of the Mannaean Kingdom as an intermediary power situated between Assyria and the polities of the Zagros Mountains. This strategic position contributed significantly to the kingdom's political influence, economic prosperity, and cultural development. By integrating archaeological evidence with regional chronology, Hassanzadeh further distinguishes the formative phases of Mannaean civilization from the subsequent period in which the kingdom became incorporated into the Median political sphere. Consequently, this study represents one of the principal references for understanding the archaeology and cultural development of the Mannaean kingdom in the northwestern Zagros. Although these studies have substantially advanced understanding of Mannaean archaeology and archaeological iron corrosion, comprehensive archaeometallurgical investigations integrating manufacturing technology, alloy characterization, microstructural analysis, and corrosion mechanisms in copper-based artifacts from Qalaichi remain lacking. The present study seeks to address this research gap through a multidisciplinary analytical approach combining metallography, SEM–EDS, XRD, and complementary archaeometallurgical methods.

Materials and Methods

This study examined nine archaeological samples recovered from Qalaichi Tepe (Fig. 1a–i).

- Methods

A multidisciplinary analytical approach was adopted to investigate the manufacturing technology, microstructural characteristics, chemical composition, and corrosion processes of archaeological metal artifacts recovered from Qalaichi Tepe. The analytical protocol comprised optical

	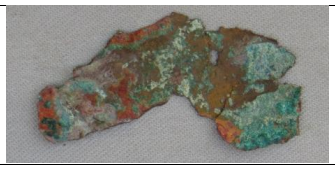	
a	b	c
Specimen: M-A-1, a ring with a diameter of 5.6 cm. Maximum thickness 0.5 cm, minimum thickness 0.23 cm. weighs 240 g.	Sample: M-A-4, weighing 7.2 g and 0.7 mm thick; its diameter is 3.9 cm at the widest point and 1.4 cm at the narrowest point.	Sample M-B-1: Weight 4 g, thickness 5 mm, length approximately 5 cm; active chlorine corrosion.
d	e	f
Sample M-B-2: Weighing 3.2 g and 0.5 mm thick, with a small, attached sheet fragment; shows blue, green, brown, and black corrosion. Dimensions: 3.5 cm in length and 2 cm in width.	Specimen M-B-3: A bronze specimen weighing 4.2 g and 0.7 mm thick; dimensions are 3.3 cm in length and 1.7 cm in width; exhibits corrosion in green, blue, brown, black, and orange hues.	Sample M-B-4: A small sheet fragment weighing 0.9 g, with a thickness of 0.5 mm, a length of 1.9 cm, and a width of 1.5 cm; showing areas of black, dark green, light green, brown, and blue corrosion.
g	h	i
Specimen M-B-5: Thickness 1.1 mm, weight 0.8 g, length 2 cm, and width 1 cm. Corrosion products appear in pale green, dark green, brown, white, and black.	Sample M-B-6: Weight 0.8 g; thickness 1 mm; dimensions 1.2 cm by 1 cm; featuring pale green powdery, white, and brown corrosion products.	Specimen M-B-7: Weighing 0.6 g with a thickness of 1.2 mm, a length of 1.6 cm, and a width of 1.3 cm; showing pale powdery green, dark green, and brown corrosion.

Fig. 1: (A–I), Nine sample fragments recovered from Qalaychi Tepe (Authors, 2025). ▶

microscopy (OM), metallographic examination, scanning electron microscopy coupled with energy-dispersive X-ray spectroscopy (SEM–EDS), and X-ray diffraction (XRD). These complementary techniques were applied to characterize the manufacturing technology, alloy composition, microstructure, corrosion products, and deterioration mechanisms of the artifacts.

Optical Microscopy (OM): Optical microscopy was initially employed as a rapid, non-destructive technique for the preliminary examination of the archaeological specimens. This approach enabled characterization of surface morphology, corrosion layers, surface deposits, and deterioration features prior to destructive sampling. Optical microscopic observations provided essential information on the preservation state of the artifacts and facilitated the selection of representative areas for subsequent analytical investigations (Stewart, 2007: 79–83).

Metallographic Examination: Metallographic analysis was performed to characterize the microstructure and manufacturing technology of the artifacts. Representative samples were mounted in epoxy resin, ground

with progressively finer silicon carbide abrasive papers, polished using diamond suspensions, and chemically etched to reveal their metallographic structure. Examination by reflected-light microscopy provided information on manufacturing processes such as casting, cold working, hot working, annealing, and other thermomechanical treatments, as well as alloy composition, grain morphology, and corrosion-induced microstructural alterations (Scott, 1991: 70–72). Metallographic observations were conducted using an OGAWA SEIKI Co., Ltd. MR-11 reflected-light metallurgical microscope at the Art University of Isfahan.

SEM–EDS: Scanning electron microscopy (SEM) was employed to examine the surface morphology and microstructural features of the archaeological metal artifacts at high magnification. Unlike optical microscopy, SEM employs a focused electron beam to generate high-resolution images of the specimen surface (Frahm, 2014). When coupled with energy-dispersive X-ray spectroscopy (EDS), SEM enables qualitative and semi-quantitative elemental analysis of both the metallic substrate and corrosion layers, providing valuable information on alloy composition, manufacturing technology, and corrosion processes. SEM–EDS analyses were conducted at the Razi Applied Science Foundation using a TESCAN MIRA3 scanning electron microscope equipped with an energy-dispersive X-ray spectroscopy (EDS) detector.

XRD: X-ray diffraction (XRD) analysis was conducted to identify the crystalline phases present in the corrosion products. As an established technique for phase identification in archaeological metals, XRD enables characterization of crystalline corrosion compounds by comparing their diffraction patterns with standard reference databases. Powdered corrosion samples were analysed using a Bruker D8 ADVANCE X-ray diffractometer (Bruker AXS, Germany) at the Central Laboratory of the University of Isfahan.

Results and Discussion

- Microstructural Characterization

Sample M-A-1: In Figure 2a (before etching), the yellowish matrix and its metallic luster are clearly visible. Several phases with distinct colors are observed within the metallic matrix, together with blue-gray regions corresponding to sulfide inclusions and intergranular corrosion products (see the SEM–EDX analysis for further details).

In the etched microstructure of the sample (Fig. 2b), recrystallized grains and annealing twins are clearly visible. In several regions, the

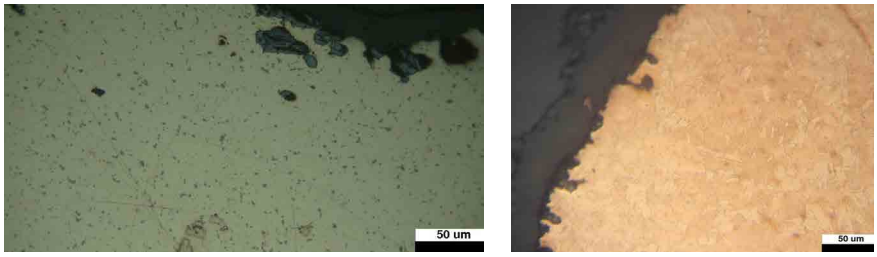

Fig. 2: Optical micrographs of sample M-A-1: (a) before etching and (b) after etching (100×). (Authors, 2025). ▶

twin boundaries exhibit a curved morphology, indicating that the object underwent multiple cycles of mechanical working and annealing during manufacture. The presence of well-developed annealing twins further suggests that annealing constituted the final stage of the manufacturing process (Scott, 1991: 5–6). Sample M-A-4: In Figure 3a, the yellowish metallic matrix and its metallic luster are clearly visible. Elongated blue-gray sulfide inclusions are distributed within the matrix. The gray and black phases correspond to intergranular and grain-boundary corrosion. Grain-boundary corrosion has progressed to such an extent that the fine-grained microstructure of the sample is clearly discernible in several areas.

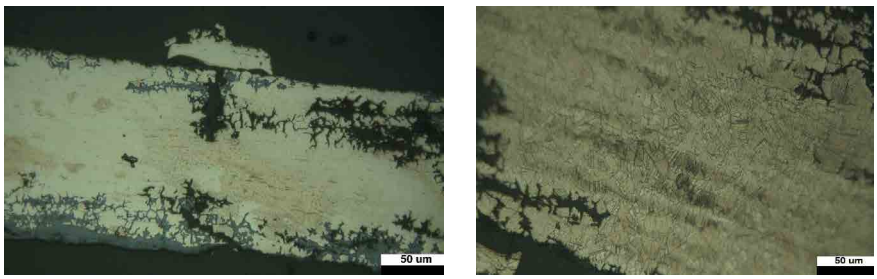

Fig. 3: Optical micrographs of sample M-A-4: (a) before etching (100×) and (b) after etching (200×), (Authors, 2025). ▶

In the etched microstructure of sample M-A-4 (Fig. 3b), recrystallized grains, annealing twins, and pronounced deformation (strain) bands are clearly observed. The twin boundaries exhibit extensive bending and fragmentation, indicating that the artifact experienced repeated cycles of mechanical working. Based on the pronounced deformation features and the morphology of the twin boundaries, the final stage of manufacture is interpreted to have been cold working (Oudbashi and Davami, 2014: 7–10).

Sample M-B-1: In Figure 4a (before etching), black and gray phases are visible together with grain-boundary and intergranular corrosion. Corrosion has progressed to such an extent that twin boundaries and deformation bands are clearly discernible in several grains.

In the etched microstructure of sample M-B-1 (Fig. 4b), recrystallized grains, annealing twins, and deformation bands are clearly observed. These microstructural features indicate that the object underwent multiple cycles of mechanical working and annealing. The presence of deformation bands

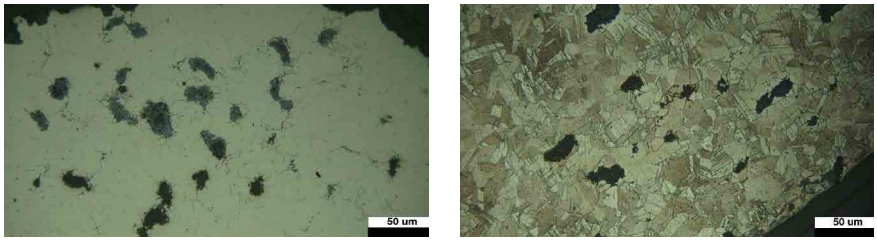

◀ Fig. 4: Metallographic micrographs of sample M-B-1: (a) before etching (100×) and (b) after etching (100×), (Authors, 2025).

within the grains further suggests that cold working constituted the final stage of manufacture. Variations in grain size across the microstructure indicate that different regions of the object were subjected to different degrees of mechanical deformation.

Sample M-B-2: In Figure 5a (before etching), the yellowish metallic matrix is clearly visible. Elongated sulfide inclusions are distributed throughout the matrix, together with abundant black intergranular corrosion products. The matrix also contains numerous fine pores. In cast metals, such porosity and voids may result from gases dissolved in the molten metal or from interdendritic shrinkage cavities that were not completely filled during solidification (Scott, 1991: 5–6).

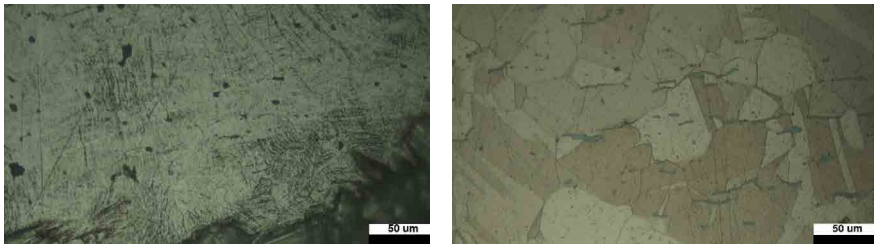

◀ Fig. 5: Metallographic micrographs of sample M-B-2: (a) before etching (200×) and (b) after etching (400×), (Authors, 2025).

In the etched microstructure of sample M-B-2 (Fig. 5b), coarse recrystallized grains and well-developed annealing twins are clearly observed. The presence of annealing twins indicates that annealing constituted the final stage of the manufacturing process. The elongated sulfide inclusions suggest that the artifact underwent repeated cycles of mechanical working, while the fragmented and distorted twin boundaries further support this interpretation. The pronounced grain coarsening indicates that the object was subjected to prolonged heat treatment at an elevated temperature, resulting in the development of a coarse-grained microstructure (Scott, 1991: 7). Sample M-B-3: In Figure 6a, the matrix exhibits a yellowish appearance with a distinct metallic luster. Blue-gray, black, and gray phases are observed throughout the microstructure. According to the SEM–EDS analysis, the elongated inclusions distributed along the matrix are identified as sulfide inclusions. In addition, intergranular and grain-boundary corrosion, together with numerous fine, rounded pores, are clear.

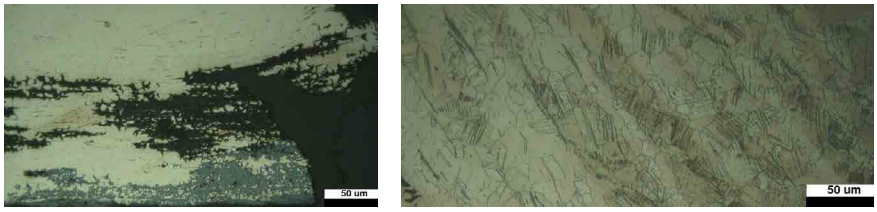

Fig. 6: (a) Metallographic micrograph of sample M-B-3 before etching, at 200×. (b) Metallographic micrograph of sample M-B-3 after etching, at 400×, (Authors, 2025). ▶

The etched microstructure of sample M-B-3 (Fig. 6b) consists of recrystallized grains, annealing twins, and deformation bands. The presence of deformation bands indicates that mechanical working constituted the final stage of the manufacturing process, suggesting that no final annealing treatment was performed. The bent and fragmented twin boundaries, together with the very fine grain structure and elongated sulfide inclusions, indicate that the artifact underwent numerous cycles of mechanical working.

Sample M-B-4: Figure 7a (before etching) reveals a metallic matrix containing gray and black phases associated with intergranular and grain-boundary corrosion. In addition, blue-gray phases corresponding to highly elongated sulfide inclusions are clearly observed.

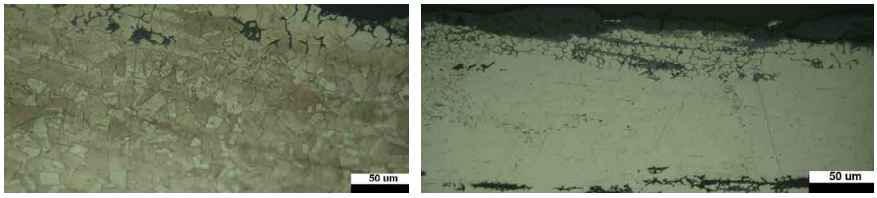

Fig. 7: (a) Metallographic micrograph of sample M-B-4 before etching, at 100× n. (b) Metallographic micrograph of sample M-B-4 after etching, at 200×. (Authors, 2025). ▶

In the etched microstructure of the sample (Fig. 7b), recrystallized grains, along with annealing twins and deformation lines, are clearly visible. In some regions, the annealing twins appear bent or discontinuous. Deformation lines observed within the grains may indicate that the artifact underwent mechanical working as the final stage of manufacture. This suggests that the object either did not undergo a final annealing treatment after deformation, or that the final annealing was insufficient to completely eliminate the deformation features. Consequently, a limited number of deformation lines remain preserved within the grains (Scott, 1991: 5–6).

Sample M-B-5: As shown in Figures 8a and 8b, the sample exhibits extensive intergranular and grain boundary corrosion throughout the entire cross-section. The high degree of corrosion has naturally revealed the deformation lines, annealing twins, and the fine-grained microstructure, effectively producing a naturally etched surface. Consequently, no additional chemical etching was required prior to metallographic examination.

At higher magnification (Fig. 8b), the grain structure is more clearly resolved. The widespread presence of deformation lines further indicates

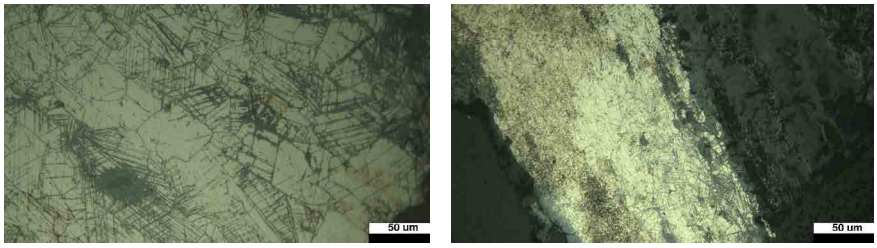

◀ Fig. 8: (a) Metallographic micrograph of sample M-B-5 in unetched condition, at 100× (b) Metallographic micrograph of sample M-B-5 in the unetched condition, at 400×. (Authors, 2025).

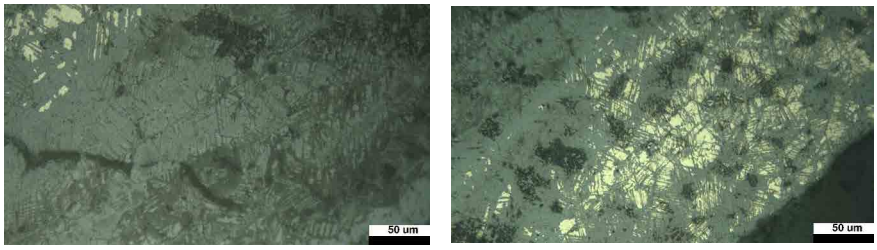

◀ Fig. 9: (a) Metallographic micrograph of sample M-B-6 in unetched condition, at 200×. (b) Metallographic micrograph of sample M-B-6 in unetched condition, at 200×. (Authors, 2025).

that mechanical working, most likely hammering, constituted the final stage of the manufacturing process. The yellow-colored phase represents remnants of the original grain structure within the metallic matrix that has not yet undergone corrosion. Extensive corrosion has preferentially attacked the grain boundaries, making them clearly distinguishable. Traces of deformation lines are also visible, suggesting that the artifact underwent mechanical working, most likely hammering, as the final stage of manufacture. Furthermore, Figure 9b illustrates that the corrosion features have effectively revealed the microstructure. In this image, the grains, grain boundaries, and corrosion-induced cracks are clearly discernible. Localized intergranular and grain boundary corrosion can be observed in several regions of the sample. The micrograph reveals gray and black corrosion products, together with the yellow-colored grains of the metallic alloy. Corrosion-induced surface features and fine cracks are also evident. P20-R20.

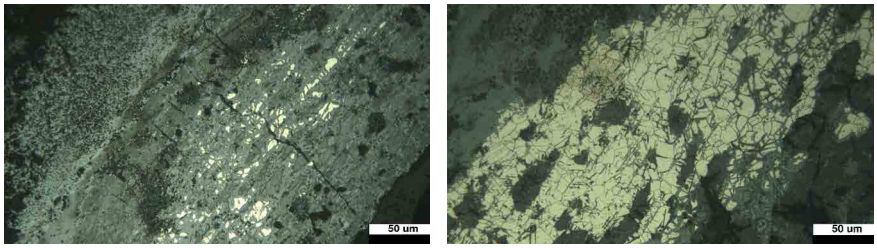

◀ Fig. 10: (a) Metallographic micrograph sample M-B-7 in unetched condition, at 200×. (b) Metallographic micrograph of sample M-B-7 in unetched condition, at 100×. (Authors, 2025).

Scanning Electron Microscopy (SEM–EDS)

Scanning electron microscopy coupled with energy-dispersive X-ray spectroscopy (SEM–EDS) was employed to perform semi-quantitative elemental analyses at selected locations on the archaeological specimens. The elemental data obtained from SEM–EDS were used to characterize the

corrosion state of the samples and to identify the distribution of the major elements within the metallic substrate and corrosion products.

MA1

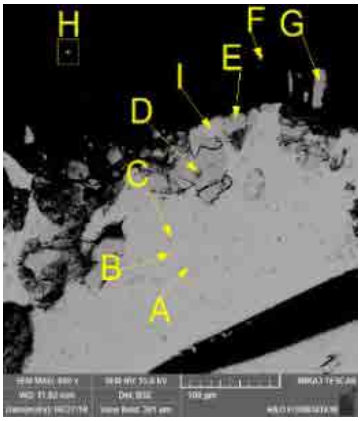

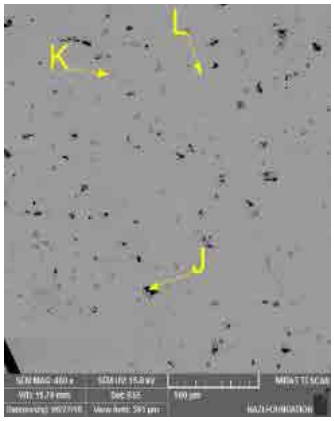

Fig. 11: SEM micrographs (a–r) and corresponding EDS elemental compositions of the studied samples, expressed as weight percentages (wt.%), (a), (Authors, 2025). ▶ Fig. 11: (b), (Authors, 2025). ▶▶

Table 1-1: Elemental analysis results of the sample expressed as weight percentages (Authors, 2025). ▶

M-A-1	A	B	C	D	E	F	G	H	I	J	K	L	M
S	1.40	1.87	17.69	1.50	1.87	0.97	4.58	0.90	2.47	10.40	20.01	1.99	0.00
C								72.79					
Cu	96.82	95.84	80.01	84.56	82.69	80.64	76.75	0.61	95.90	86.77	76.81	95.62	45.00
Zn	0.47	0.63	0.60	0.67	0.50	0.45	0.46	0.51	0.49	0.54	0.54	0.65	1.01
Sn	1.31	1.18	0.85	0.52	0.69	0.77	1.57	0.34	0.99	1.18	0.92	0.76	1.34
Pb		0.48			0.00	0.75	2.46	0.00	0.00			0.68	52.23
Fe			0.84	0.14	0.12	0.15	0.13	0.20	0.15	0.78	1.72	0.29	0.42
O				12.61	14.11	14.49	12.44	24.47					
Cl						1.78	1.60	0.18		0.32			

MA4

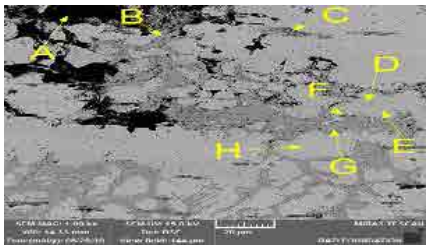

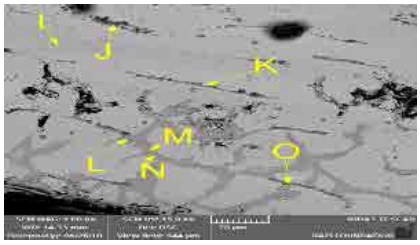

Fig. 11: (c), (Authors, 2025). ▶
Fig. 11: (d), (Authors, 2025). ▶▶

Table 1-2: Elemental analysis results expressed as weight percentages (wt.%), (Authors, 2025). ▶

M-A-4	A	B	C	D	E	F	G	H	I	J	K	L	M	N	O	P
C	58.78					54.40										
O	6.77	17.31	8.05	3.89	20.29	5.42	19.28			8.97		15.49	21.99	20.67	10.69	14.28
S	0.97	0.77	13.99		2.50	1.44	1.47	1.30	0.57	9.54	17.06	0.54	0.73	0.85	7.59	1.03
Ca					7.07	0.00										
P						0.23										
Cu	9.78	56.23	75.38	88.25	62.36	32.43	57.70	86.05	89.97	76.35	79.10	80.75	44.64	48.92	77.45	67.39
Zn	0.76	0.42	0.43	0.68	0.62	0.43	0.58	0.51	0.60	0.86	0.81	0.56	0.53	0.75	0.69	0.45
Sn	22.59	22.28	1.93	6.98	6.91	5.50	20.73	11.98	6.97	3.93	2.81	2.54	31.81	28.30	3.34	16.71
Fe	0.36	0.27	0.22	0.20	0.25	0.17	0.23	0.16	0.22	0.35	0.22	0.12	0.31	0.50	0.24	0.15
Pb		2.72						0.00	1.68							

MB1

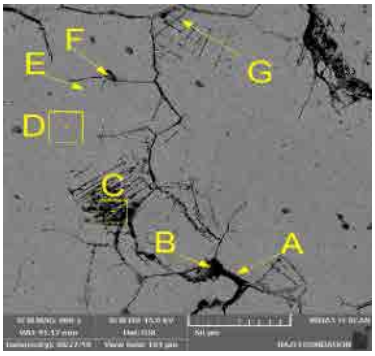

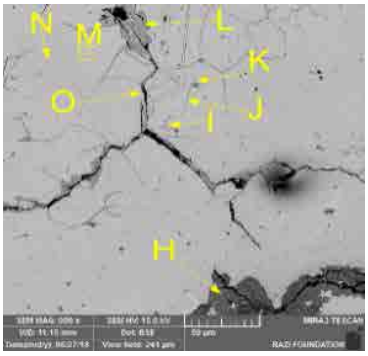

◀Fig. 11: (e), (Authors, 2025).
◀◀Fig. 11: (f), (Authors, 2025).

M-B-1	A	B	C	D	E	F	G	H	I	J	K	L	M	N	O	P	Q
C	21.12	32.77			50.77									55.74	56.39		
O	1.12	3.52	13.94				13.26	34.21	12.91	11.29		16.22			3.18		
S	0.00	0.85	1.42	2.09	1.94	18.35	1.57	1.20	1.90	2.13	7.63	1.80	2.25	1.55	0.22	0.82	0.32
Cl	0.04	0.25	0.81														
Cu	66.35	46.57	44.78	81.99	38.40	79.17	78.32	26.09	70.88	70.80	88.97	57.39	79.98	36.12	35.26	4.26	37.36
Zn	0.62	0.39	0.33	0.40	0.20	0.55	0.50	0.34	0.46	0.29	0.77	0.37	0.56	0.28	0.32	0.37	0.71
Sn	10.74	15.67	36.29	15.52	8.05	1.93	6.35	35.17	13.85	15.49	2.62	22.36	17.21	6.31	4.64	2.42	10.06
Pb	0.00	0.00	2.43	0.00	0.63		0.00	0.00	0.00	0.00		1.85	0.00	0.00	0.00	0.00	51.54
Si								0.86									
Ag																92.12	
P								2.13									

◀ Table 1-3: Elemental analysis results expressed as weight percentages (wt.%), (Authors, 2025).

MB2

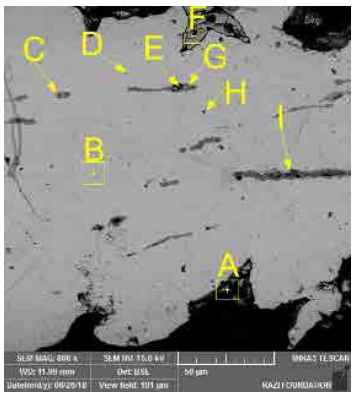

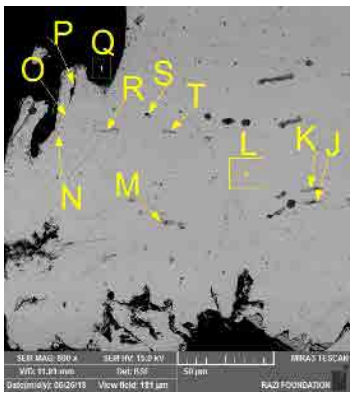

◀Fig. 11: (g), (Authors, 2025).
◀◀Fig. 11: (h), (Authors, 2025).

M-B-2	A	B	C	D	E	F	G	H	I	J	K	L	M	N	O	P	Q
C	57.29			42.50	51.07									35.84	16.02	54.67	29.21
O	14.09		8.47		4.73	12.41		23.16		22.09							
S	1.41	0.63	9.60	1.13	4.15	0.94	18.04	1.41	12.85	6.22	19.33	0.40	19.92	1.13	1.25	0.60	0.68
Fe								43.95	0.21	43.12	0..22	0.11	0.13	0.08	0.07	0.11	0.24
CU	25.85	93.59	74.18	54.76	37.05	84.23	80.09	28.30	85.26	27.06	78.62	95.09	78.41	61.08	80.33	43.88	68.98
Zn	0.20	0.71	0.31	0.39	0.18	0.52	0.37	0.38	0.69	0.34	0.82	0.73	0.50	0.54	0.53	0.33	0.63
Sn	1.17	2.62	2.19	1.21	0.84	1.89	1.49	0.76	0.98	1.17	1.00	1.39	1.05	0.86	1.37	0.42	0.26
Pb	0.00	2.45	5.25	0.00	1.99	0.00		2.04		0.00		2.29		0.46	0.43	0.00	0.00

◀ Table 1-4: Elemental analysis results expressed as weight percentages (wt.%), (Authors, 2025).

MB3

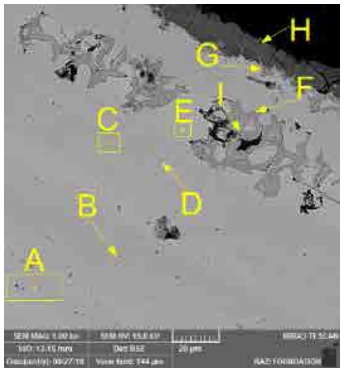

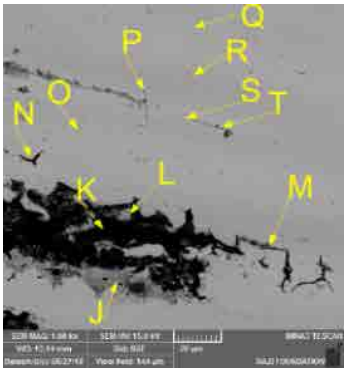

Fig. 11: (i), (Authors, 2025). ▶
Fig. 11: (j), (Authors, 2025). ▶▶

Table 1-5: Elemental analysis results expressed as weight percentages (wt.%), (Authors, 2025). ▶

MB-3	A	B	C	D	E	F	G	H	I	J	K	L	M	N	O	P	Q	R	S	T
C				37.02							64.50			52.04		55.50		44.72		
O						15.85	12.36	34.95	13.68	16.93	13.50									
S	0.67	10.95	0.62	1.18	0.18	0.43	0.28	0.57	5.42	0.84	0.41	1.02	17.25	0.37	10.34	1.50	1.34	0.20	1.59	18.19
Si								1.45												
Cl							1.86	0.60		0.73	0.87	0.86	1.04	0.03	0.23	0.23	0.31	0.18	0.36	0.41
Fe															3.39	0.12	0.13	0.13	0.23	1.23
Cu	85.41	83.42	88.10	55.52	84.45	73.45	71.88	36.86	47.57	68.54	16.00	86.87	76.40	42.92	79.78	55.15	86.42	49.42	84.11	77.41
Zn	0.89	0.62	0.62	0.62	0.65	0.62	0.35	0.42	0.32	0.55	0.60	0.67	0.62	0.36	0.61	0.39	0.39	0.41	0.54	0.47
Sn	12.51	5.01	9.14	5.61	12.05	8.65	6.91	25.69	27.65	10.60	4.02	9.54	2.68	4.29	5.67	4.23	11.42	4.13	10.85	2.28
Pb	0.55		1.52	0.00	2.66	1.00	1.37	1.62	5.36	1.81	0.50	1.04		0.00		2.87	0.00	0.81	2.53	

MB4

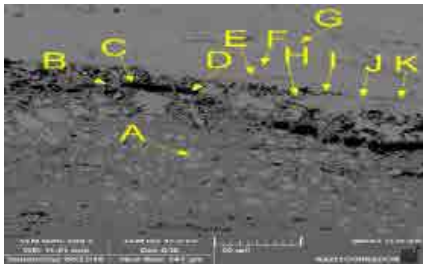

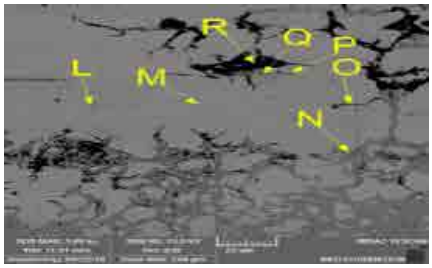

Fig. 11: (k), (Authors, 2025). ▶
Fig. 11: (l), (Authors, 2025). ▶▶

Table 1-6: Elemental analysis results expressed as weight percentages (wt.%). (Authors, 2025). ▶

MB-4	A	D	C	D	E	F	G	H	I	J	K	L	M	N	O	P	Q	R
Si	0.44	0.45	0.00	0.03														
S	0.83	2.13	0.00	0.06	13.24	1.28	1.31	0.86	3.15	12.61	15.10	5.74	13.18	1.96	8.40	1.05	8.69	0.84
C			45.73	56.75		47.35	29.88											37.13
O			1.34	4.61				16.36						16.50		10.50		7.42
Ca			0.08	0.06														
Cl				0.34				0.78	0.05									
Fe													2.22	0.34				
Cu	84.61	80.34	51.61	37.40	81.75	45.16	61.04	63.56	74.25	80.57	79.93	84.94	79.42	62.50	83.46	56.42	84.41	29.50
Zn	0.44	0.79	0.68	0.26		0.39	0.35	0.44	0.55	0.74	0.85	0.81	0.48	0.57	0.50	0.28	0.62	0.35
Sn	11.82	15.99	0.56	0.42	5.01	5.43	5.66	17.34	22.00	6.05	4.14	8.52	4.71	18.52	7.04	30.71	6.08	24.79
Pb	2.03	0.00	0.00	0.00		0.41	1.75	0.69	0.00					0.00		1.04		0.00

MB5

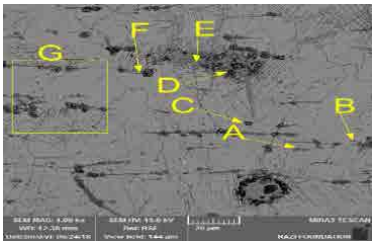

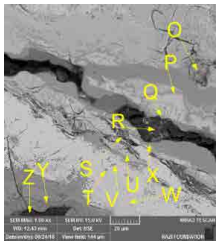

◀Fig. 11: (m), (Authors, 2025).
◀◀Fig. 11: (n), (Authors, 2025).

M-B-5	A	A1	B	B1	C	C1	D	D1	E	E1	F	F1	G	H	I	J
C		24.07		28.04											29.85	
O		20.54	9.71	18.87	10.52	13.85	16.46	12.04	23.08					13.46	13.43	36.32
S	16.04	0.51		0.41	2.34		1.19		0.37	19.08	13.16	0.00	0.78	0.22	0.30	0.31
P	0.13	1.56	1.89	1.83	0.39		0.95		1.07		0.27		0.40	0.75	2.34	6.28
Si	0.00	1.56	0.45	0.91	0.27	0.29	0.58	0.05	0.35		0.11		0.24	0.19	1.55	1.08
Fe		0.28		0.31			1.01		0.95							
K																
Ca		1.23		1.22	2.02		0.00		0.00							
Cl		0.27		0.22												
Cu	79.34	8.78	63.50	12.93	77.26	84.43	48.36	86.61	33.07	76.67	77.36	0.00	80.23	81.25	3.53	13.12
Zn	0.30	0.37	0.54	0.44	0.67	0.64	0.55	0.84	0.35	0.86	0.74	0.00	0.52	0.57	0.48	0.46
Sn	3.99	40.83	20.28	34.83	3.18	0.79	29.02	0.46	35.81	3.39	6.36	0.00	16.10	1.50	55.03	39.59
Pb			3.44		3.35		2.11		2.93				1.75	2.07	1.49	2.64

	K	L	M	N	O	P	Q	R	S	T	U	V	W	X	Y	Z
C			68.99		33.26			36.43	31.18							73.63
O	18.13	36.38	10.03		16.60	36.11	32.31	9.63	22.57	23.47	34.88	27.38	13.70	43.50	33.23	16.14
S	0.19	0.38	3.39	1.60	0.24	0.21	0.42	0.61	1.85	1.35	1.09	2.19		0.42	0.42	0.16
P	0.93	6.63	0.47	1.30	4.88	1.85	2.03	0.50	0.82	4.99	4.14	1.25		1.16	13.70	2.65
Si	0.34	1.27	0.19	0.44	0.62	0.64	0.97	0.14	0.29	0.60	0.96	0.07	0.68	0.31	0.20	0.07
Fe										0.17	0.52	0.11	0.13		0.13	0.21
K															1.48	0.00
Ca									0.35	1.40		0.11		0.40	4.88	0.25
Cl										1.95		5.28			4.37	0.16
Cu	75.85	10.07	13.88	70.23	12.23	38.26	33.28	11.05	35.88	65.21	22.03	62.64	83.98	39.13	38.56	5.30
Zn	0.63	0.42	0.66	0.42	0.41	0.36	0.50	20.01	0.33	0.55	0.43	0.58	0.61	0.43	0.60	1.03
Sn	2.64	42.10	2.39	24.30	30.15	21.14	29.07	0.78	6.74	0.32	34.40	0.34	0.91	12.52	0.24	0.39
Pb	1.30	2.75	0.00	1.81	1.62	1.45	1.42	0.85	0.00		1.55			1.93		

◀ Table 1-7: Elemental analysis results expressed as weight percentages (wt.%). (Authors, 2025).

MB6

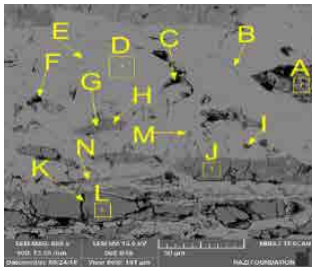

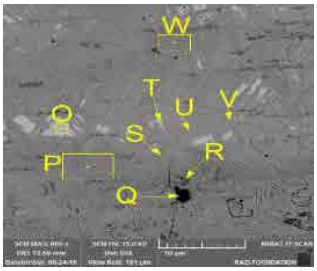

◀Fig. 11: (o), (Authors, 2025).
◀◀Fig. 11: (p), (Authors, 2025).

M-B-6	A	A1	B	B1	C	C1	D	D1	E	E1	F	G	H	I	J	K
C					67.18						66.49	24.41				
O	32.73		10.94		6.29			40.70		46.82	5.36	25.37	38.47	11.55	37.02	34.22
S	0.64	0.10	0.00	14.45	0.02	0.81	0.23	0.36	0.25	0.36	0.11	2.32	0.35	0.00	0.49	0.55
Si	1.83	0.40	0.08	0.48	0.00	0.74	0.55	10.96	0.51	6.15	0.07	1.26	1.11	0.22	1.72	0.95
P	4.06	0.54	1.29	0.99	0.18	1.82	0.70	1.10	0.76	9.39	0.30	3.59	6.35	1.18	5.43	5.86
Ca										5.39						
Cu	11.65	79.00	84.30	72.32	6.23	59.38	93.88	41.31	93.22	29.86	26.78	14.86	11.54	83.25	12.53	13.80
Zn	0.22	0.50	0.72	062	0.10	0.74	0.49	0.36	0.61	0.40	0.35	0.34	0.42	0.54	0.37	0.59
Sn	46.82	17.26	1.21	11.14	0.02	36.32	1.36	3.59	1.53	1.16	0.24	28.34	37.54	1.33	39.31	42.29
Pb	2.05	2.21	1.46		0.00		2.80	1.61	2.72	1.97	0.30	0.00	4.22	1.93	3.31	1.75

M-B-6	L	M	N	O	P	Q	R	S	T	U	V	W	X	Y	Z
C						39.33				39.00	21.54				
O	39.44	14.04			23.43	12.79	23.52	28.30		12.21	15.91	24.26		23.57	14.44
S	0.31	0.00	17.96	1.83	0.97	0.35	0.78	0.32	0.18	0.06	0.80	0.30	17.63	0.51	10.02
Si	1.15	0.18			0.88	0.80	2.06	1.14	0.39	0.17	0.26	0.94		1.08	0.82
P	6.50	1.17					2.68	1.51	0.66	0.32	0.30	1.21		1.24	1.12
Ca															
Cu	11.66	81.63	82.04	81.91	48.52	12.16	18.29	29.98	81.64	37.79	45.87	43.81	76.16	46.88	61.20
Zn	0.43	0.57		0.46	0.69	0.60	0.39	0.49	0.58	0.31	0.30	0.39		0.51	0.47
Sn	37.87	0.82		15.81	23.75	32.39	50.32	35.93	13.84	8.71	13.28	26.53	6.21	24.43	12.05
Pb	2.64	1.58		0.00	1.77	1.55	1.56	2.32	2.71	1.41	1.73	2.55		1.79	0.00

◀ Table 1-8: Elemental analysis results expressed as weight percentages (wt.%). (Authors, 2025).

MB7

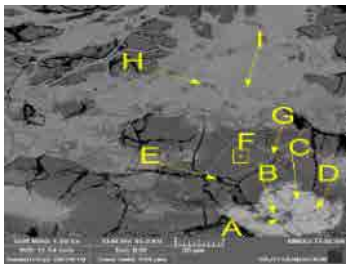

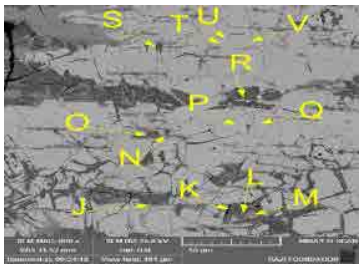

Fig. 11: (q), (Authors, 2025). ▶
Fig. 11: (r), (Authors, 2025). ▶▶

Table 1-9: Elemental analysis results expressed as weight percentages (wt.%), (Authors, 2025). ▶

MB-7	A	A1	B	B1	C	C1	D	D1	E	E1	F	G	H	I	J	K
C									35.36							
O		32.63		35.03	17.60		18.80	26.47	20.97		37.36					34.48
S	34.31	0.25	0.79	0.32	0.10	0.33	0.40	0.10	2.14	0.00	0.30	21.66	11.56	0.00	17.81	0.22
Si	0.37	1.95	0.22	2.45	0.67	0.92	0.15	2.26	0.60	0.43	1.36	0.37	0.73	0.47	0.32	1.02
P		3.57		3.99		1.60		0.99	2.90	0.42	5.81	0.59	1.04	1.68	0.63	7.10
Cl										6.23						
Cu	78.76	12.53	82.43	8.77	55.83	81.27	53.18	35.63	15.45	13.28	8.45	73.76	65.11	92.55	77.82	12.05
Zn	0.70	0.60	0.52	0.49	0.61	0.47	0.53	0.33	0.32	0.35	0.35	0.60	0.66	0.42	0.56	0.46
Sn	5.86	46.69	14.26	46.07	23.74	12.12	26.33	31.08	29.23	6.03	43.75	3.01	20.85	1.96	2.85	41.77
Pb		1.80	1.88	2.88	1.43	3.29	0.22	3.14	0.00	73.20	2.62			2.92		2.89

MB-7	L	M	N	O	P	Q	R	S	T	U	V	W	X	Y	Z
C															
O	27.76	23.64	5.13	27.03				20.18		10.11					
S	0.74	0.37	16.23	0.62	0.74	0.56	0.65	0.82	0.60	0.44	0.73	0.66	0.38	0.31	0.14
Si	1.36	1.92	0.17	0.79	0.54	0.18	2.13	0.54	0.29	0.12	0.21	0.51	1.25	0.25	0.16
P	3.12	0.73	0.34	5.51	0.40	0.20	9.25	4.95	0.35	0.29	0.36	0.54	0.66	0.30	0.33
Cl															
Cu	31.15	43.15	75.86	25.42	79.43	79.86	22.45	34.71	81.24	67.15	81.42	79.71	64.70	82.20	82.08
Zn	0.34	0.36	0.63	0.43	0.74	0.73	0.56	0.51	0.44	0.51	0.47	0.52	0.55	0.46	0.52
Sn	33.58	27.05	1.63	38.35	16.32	16.51	60.98	35.59	14.69	19.16	15.29	16.31	30.29	14.76	15.06
Pb	1.97	2.78		1.86	2.04	1.96	3.98	2.69	2.38	2.22	1.52	2.14	2.18	1.75	1.66

Sample M-A-1. Inclusions, corrosion products, lead globules, pores, and cracks are visible in Figure 11a, b. The backscattered electron (BSE) images exhibit a range of gray, black, and white tonal contrasts (Fig. 11a, b). EDS point analyses identified the chemical composition of the different regions of the specimen (Table 1-1). Point analysis at locations A, B, I, and L indicate that the metallic matrix consists predominantly of copper. The tin content is very low, occurring only in trace amounts, which most likely reflects its natural presence in the original copper ore rather than intentional alloying. These points also exhibit consistently high copper concentrations, with only minor variations between them. Small amounts of zinc and lead were also detected and are interpreted as naturally occurring impurities derived from the original ore. Point analyses at locations C, J, and K, corresponding to the dark gray inclusions, revealed the presence of copper and sulfur as the principal elements. This elemental composition is consistent with sulfide inclusions, suggesting that sulfide copper ores may have been used during smelting (Fig. 11b). The black regions at points D, E, F, and G contain significant amounts of copper together with relatively high oxygen concentrations. The decrease in copper content accompanied by an increase in oxygen is indicative of corrosion processes affecting these

areas. Furthermore, chlorine was detected at points F and G, most likely reflecting the influence of the burial environment and its role in promoting corrosion. Trace amounts of zinc, tin, lead, and iron were also identified at these locations, which are likewise interpreted as natural impurities inherited from the original ore (Craddock, 1995: 243).

Sample M-A-4. Fine corrosion-induced cracks and inclusions are visible in Figures 11c and 11d. EDS analyses indicate that the principal elements detected at points A and F are carbon, oxygen, copper, and tin. The high carbon content, together with the marked depletion of copper and the presence of oxygen, indicates that active corrosion processes have occurred in these regions. Minor amounts of iron, zinc, sulfur, and phosphorus were also identified. Iron, zinc, and sulfur most likely originated as natural impurities in the original ore or were present as minor alloying constituents. The chemical compositions at points D, H, and I indicate that the metallic matrix is a bronze alloy. The high copper content accompanied by significant amounts of tin confirms the bronze composition of the alloy. Oxygen detected at point D may be associated with the initial stages of corrosion or surface alteration. Trace amounts of lead, iron, and zinc were also detected at these locations and are interpreted as impurities originating from the primary ore. The EDS analyses at points B, E, G, M, N, and P show a similar elemental composition, although with some variation in elemental concentrations. In these regions, the decrease in copper, accompanied by increased oxygen and tin contents, clearly reflects the effects of corrosion. Trace quantities of lead, iron, zinc, and sulfur were likewise identified and are attributed either to primary ore impurities or to the incorporation of foreign materials during the smelting process. The chemical composition at point L is comparable to that of the other regions, except that the tin concentration is relatively lower. The high copper content, together with the presence of oxygen, indicates the occurrence of surface corrosion in this area. The gray regions at points C, J, K, and O are characterized by high sulfur concentrations coupled with elevated copper contents. This elemental composition is most likely attributable to sulfide inclusions retained from the original copper ore or to incompletely reduced sulfide residues that became elongated within the metallic matrix during subsequent thermomechanical processing (Rostoker *et al.,* 1989: 69–87).

Sample M-B-1. Cracks, intergranular corrosion, and strain lines adjacent to corrosion cracks within the metallic matrix are visible in Figures 11e and 11f. EDS analyses of the black regions at points A, B, N, and O (Table 1-3) indicate similar chemical compositions. The principal

elements detected at these locations are copper, tin, and carbon. The high carbon content most likely derives from the epoxy mounting resin, carbon coating applied for SEM analysis, or carbonaceous contamination associated with corrosion products. Accordingly, the carbon signal should not be interpreted quantitatively or regarded as representative of the alloy composition. Oxygen was detected only in minor amounts, primarily at points A, B, and O. In addition, trace amounts of chlorine, sulfur, zinc, and lead were identified and are most likely attributable to impurities inherited from the original ore or introduced during metallurgical processing. Points C, G, H, I, J, and L also exhibit relatively uniform elemental compositions. The elevated oxygen and tin contents, accompanied by a decrease in copper, indicate advanced corrosion in these regions. This pattern may be attributed to the selective dissolution of copper and its migration into the surrounding environment, while the relative stability of tin under burial conditions results in its apparent enrichment within the alloy (Robbiola *et al.,* 1998: 2083–2111). At point C, a relatively high concentration of lead was detected. Minor amounts of chlorine, sulfur, and zinc were also present in these regions, most likely reflecting impurities derived from the original ore or introduced during metal extraction and smelting. Points D and M represent the primary metallic matrix of the specimen and exhibit high concentrations of copper and tin, confirming the bronze composition of the alloy. In contrast, points F and K contain significant concentrations of sulfur and copper, indicating the presence of sulfide inclusions within the alloy. The small amount of tin detected in these areas may reflect analysis across the interface between the sulfide inclusion and the surrounding metallic matrix. At point P, silver was identified as the dominant element, suggesting that it was retained as a natural impurity originating from the primary ore. Finally, point Q, characterized by a high lead content together with appreciable amounts of tin and copper, was identified as a lead globule. Such globules likely result from localized phase segregation during alloy solidification or represent remnants of the ancient smelting process (Scott, 1991: 23–24).

Sample M-B-2. Extensive corrosion, abundant porosity, and elongated inclusions are visible in Figures 11g and 11h. EDS point analyses of the black regions (points A, D, E, N, O, P, and Q) reveal high carbon contents accompanied by a marked depletion of copper in areas showing advanced corrosion of the metallic matrix. The elevated carbon signal is most likely attributable to the epoxy mounting resin, carbon coating applied for SEM examination, or carbonaceous contamination associated with the corrosion

products and should therefore not be interpreted quantitatively. At points A and E, elevated oxygen concentrations were also detected, further supporting the interpretation that oxidative corrosion processes played a major role in the deterioration of the metallic matrix. In contrast, analyses of points B and L, corresponding to the light-gray matrix, indicate that these regions consist predominantly of high-purity copper. Only trace amounts of tin were detected, indicating that the composition in these areas is consistent with a low-tin bronze. Points G, I, K, and M, which correspond to dark-gray inclusions, are characterized by high concentrations of sulfur and copper. This elemental association suggests the presence of copper sulfide inclusions, most likely retained following incomplete reduction of sulfide ores during smelting. Points H and J exhibit elevated concentrations of iron, oxygen, and copper, indicating advanced corrosion associated with iron-bearing phases. In particular, the high iron and oxygen contents, together with the depletion of copper, suggest ionic migration and secondary alteration processes within the burial environment. At point C, the coexistence of oxygen, sulfur, copper, and lead indicates a complex inclusion containing residual ore-derived phases. Point F, characterized by copper and oxygen, represents an area affected by oxidative copper corrosion, where the metallic surface has undergone direct oxidation. Overall, the SEM–EDS results demonstrate considerable variability in both the corrosion features and mineral inclusions within the specimen. These differences are attributable to the burial environment, the mineralogical characteristics of the original ore, and the efficiency of the ancient smelting process (Table 1-4).

Sample M-B-3. Advanced corrosion and numerous inclusions are evident in Figures 11i and 11j. EDS analyses of points A, C, E, L, Q, and S indicate that copper and tin are the predominant elements, confirming the bronze composition of the specimen. These regions contain high copper concentrations and moderate tin contents, consistent with compositions commonly reported for archaeological bronze alloys. Minor amounts of sulfur, zinc, and lead were also detected. These elements most likely originated as natural impurities in the primary ore or were incorporated into the metallic matrix during the smelting process. Points B, M, and T, which appear as elongated dark-gray inclusions, are characterized by relatively high concentrations of sulfur and copper. This elemental association is indicative of copper sulfide inclusions, suggesting that part of the sulfidic ore was incompletely reduced during smelting and therefore remained preserved within the alloy microstructure (Scott, 2002: 145–164). Trace

amounts of tin and zinc were also detected in these inclusions, reflecting either the original ore composition or the preferential stability of these elements within specific phases. Point analyses of D, K, N, P, and R reveal elevated carbon contents accompanied by marked depletion of copper and tin, indicating areas that have undergone significant corrosion. These regions were most likely altered by post-depositional chemical processes, resulting in the partial leaching of the principal metallic constituents from the alloy. A similar pattern is observed at points F, G, H, and J, where increased oxygen concentrations, together with copper depletion and relative enrichment in tin, suggest selective dissolution (decuprification) of copper and the consequent relative enrichment of tin during long-term burial. This corrosion mechanism has been widely documented in archaeological bronzes subjected to prolonged burial conditions. At point M, the coexistence of copper, tin, and a high sulfur concentration further support the presence of sulfide inclusions within the alloy. Iron was also detected at points D, P, Q, R, S, and T. Had the iron concentration been substantially higher, the original ore might have been identified as chalcopyrite ($CuFeS_2$). However, the relatively low iron concentrations observed in these regions are more reasonably interpreted as residual impurities inherited from the primary ore during the ancient smelting process (Bakhshandehfard, 2010: 151).

Sample M-B-4. The microstructure shown in Figures 11k and 11l exhibits intergranular corrosion, numerous microcracks, and fine porosity. EDS analyses of points A, B, and I revealed high concentrations of copper and tin, characteristic of bronze alloys and confirming the bronze composition of the specimen. In addition to these major constituents, trace amounts of sulfur, zinc, and lead were detected, which are interpreted as impurities inherited from the original ore or introduced during the smelting process. In contrast, points C, D, F, G, and R are characterized by elevated carbon contents and a pronounced depletion of copper, a compositional pattern consistent with corrosion. Significant amounts of tin were detected at points F, G, and R, whereas tin was present only in trace quantities at points C and D. Minor concentrations of calcium, chlorine, sulfur, silicon, and lead were also identified at these two locations. Since calcium, chlorine, and silicon are commonly associated with mineral phases, these elements were most likely incorporated into the analyzed material from the surrounding burial environment. Points E, J, K, L, M, O, and Q exhibit elemental associations of copper, tin, and sulfur, indicating the presence of sulfide inclusions within the matrix. The high copper concentrations,

together with moderate sulfur and tin contents and only trace levels of zinc (<1 wt.%), suggest a relatively high-purity bronze alloy containing residual sulfide inclusions inherited from the smelting process. At points H, N, and P, elevated oxygen concentrations accompanied by copper depletion and relative tin enrichment indicate the occurrence of oxidative corrosion and selective dissolution (decuprification) of copper. These corrosion features are consistent with prolonged interaction with the burial environment, particularly under chloride-rich conditions. The presence of chlorine at these locations suggests that chloride ions played an important role in accelerating the deterioration of the matrix. Overall, the results summarized in Table 1-6 demonstrate considerable variability in both the type and severity of corrosion throughout the specimen. They also provide evidence for the preservation of mineral inclusions originating from the primary ore, as well as chemical alterations resulting from long-term interaction with the burial environment.

Sample M-B-5. Extensive corrosion features and numerous microcracks are visible in Figures 11m and 11n. EDS analyses of points A, E1, and F reveal the presence of dark inclusions enriched in sulfur and copper. These regions correspond to copper sulfide inclusions, indicating that the sulfide ore was not completely reduced to metallic copper during the smelting process and consequently remained within the alloy as residual mineral phases. More specifically, these inclusions reflect the incomplete reduction of copper sulfides within ancient smelting furnaces. Appreciable amounts of tin were also detected at these locations, confirming that the object was manufactured from a bronze alloy. Minor quantities of zinc, silicon, and phosphorus were likewise identified. Points A1, B1, I, M, O, R, S, and Z exhibit similar elemental compositions. Compared with the metallic matrix, these regions are characterized by a marked depletion of copper accompanied by enrichment in carbon, oxygen, and, in most cases, tin. This compositional pattern is indicative of long-term corrosion processes under burial conditions. Such alterations are consistent with the selective dissolution (decuprification) of copper and its migration from the alloy, coupled with the relative enrichment and stabilization of tin in the form of tin oxides or residual metallic tin. This phenomenon has been widely described in the archaeometallurgical literature as secondary tin enrichment (Robbiola *et al.,* 1998). The occurrence of minor elements, including lead, zinc, phosphorus, sulfur, and silicon, further indicates the presence of primary ore-derived impurities retained within the alloy. Point Y exhibits a more complex elemental composition, including oxygen, phosphorus, calcium, chlorine, and copper. Some of these elements, particularly

phosphorus and calcium, were most likely introduced through prolonged interaction with burial soil and associated geochemical processes. The presence of chlorine at this location is particularly significant, as chloride ions are known to accelerate the corrosion of archaeological copper alloys, thereby contributing to the progressive structural deterioration of the artifact (Selwyn, 2006: 306–322).

Sample M-B-6. Corrosion features, microcracks, strain lines, and inclusions are clearly visible in Figures 11o and 11p. EDS analyses of points A, H, J, K, L, P, R, S, W, and Y (Table 1-8) identified oxygen, copper, and tin as the principal elements. The elevated oxygen contents, together with the depletion of copper and the relative enrichment of tin in several regions, are characteristic of oxidative corrosion and selective dissolution (decuprification) of copper during long-term burial. At points A1, C1, O, and T, the elemental composition is dominated by copper and tin, confirming that the artifact was manufactured from a tin bronze alloy. In contrast, points B1, N, and X exhibit elevated concentrations of sulfur and copper, indicating the presence of copper sulfide inclusions retained as residual ore-derived phases owing to the incomplete reduction of sulfidic copper ores during ancient smelting. Such inclusions are commonly observed in archaeological copper alloys and provide valuable evidence for reconstructing ancient metallurgical practices and identifying the nature of the raw materials used.

Sample M-B-7. Corroded regions associated with numerous microcracks are visible in Figures 11q and 11r. Points A, G, H, and J correspond to dark-gray copper sulfide inclusions. The high sulfur and copper concentrations detected at these locations indicate the preservation of residual copper sulfide inclusions within the alloy microstructure, reflecting incomplete reduction of sulfidic copper ores during smelting. EDS analyses of points A1, B1, C, D, D1, F, K, L, M, O, S, and U identified oxygen, copper, and tin as the principal elements. The elevated oxygen concentrations, accompanied by marked copper depletion and relative tin enrichment, are consistent with oxidative corrosion and selective dissolution (decuprification) of copper during prolonged burial. In contrast, points B, C1, P, Q, R, T, V, W, X, Y, and Z are dominated by copper and tin, confirming that the object was manufactured from a tin bronze alloy. Overall, the elemental distributions indicate that the specimen underwent extensive post-depositional alteration while retaining clear evidence of its original alloy composition, manufacturing technology, and residual ore-derived sulfide inclusions.

X-ray Diffraction (XRD)

The XRD results obtained for the corrosion products of the investigated samples are summarized in Table 2. The corrosion products of sample M-A-1 could not be identified because the corrosion layers had been removed before analysis, precluding XRD characterization. XRD analysis revealed that sample M-A-4 contained the corrosion phases cuprite (Cu_2O), nantokite (CuCl), and brochantite ($Cu_4SO_4(OH)_6$). In sample M-B-1, the corrosion products and associated burial deposits were identified as cuprite and gypsum ($CaSO_4 \cdot 2H_2O$). Sample M-B-2 yielded brochantite, cuprite, and malachite ($Cu_2CO_3(OH)_2$), whereas samples M-B-3 and M-B-4 exhibited cuprite, nantokite, and brochantite as the principal corrosion phases. In samples M-B-5, M-B-6, and M-B-7, the identified corrosion products comprised cuprite, brochantite, and malachite. Cuprite, a red to reddish-orange copper(I) oxide (Cu_2O), is typically among the earliest corrosion products to form on archaeological copper alloys. It develops as a relatively compact inner layer directly on the metallic surface and acts as a partially protective barrier that retards further oxidation. By contrast, nantokite (CuCl) is a metastable copper(I) chloride whose presence is generally regarded as a diagnostic indicator of active chloride-induced corrosion, commonly referred to as bronze disease (Bakhshandehfard, 2010: 163). Malachite, a basic copper carbonate, is among the most common and stable corrosion products observed on archaeological bronzes recovered from burial environments (Scott, 2002: 102–108). Brochantite, a green basic copper sulfate, is another stable secondary corrosion mineral that commonly forms on copper alloys exposed to oxygenated, sulfate-bearing environments. Quantitative elemental characterization of samples M-B-5, M-B-6, and M-B-7 was limited because these specimens had undergone extensive corrosion, resulting in substantial alteration of the original metallic matrix.

This conclusion is supported by both the SEM–EDS and metallographic observations, which demonstrate advanced degradation and extensive replacement of the original alloy by corrosion products.

Comparative Review of Metallurgical Studies at Qalaichi Tepe

To date, three independent studies have investigated the metallic artifacts recovered from the Qalaichi archaeological site. Bahadari examined the iron artifacts, Soudagar investigated a collection of bronze and iron objects, and the present study focuses on a group of bronze artifacts.

Table 2: XRD identification of the corrosion products detected in the archaeological metal samples investigated in this study (Authors, 2025). ▼

Sample	XRD Pattern	Gypsum	Brochantite	Nantokite	Malachite	Tenorite	Cuprite
M-A-4	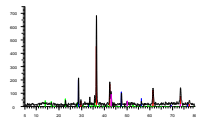	–	+	+	–	–	+
M-B-1	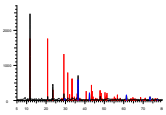	+	–	–	–	–	+
M-B-2	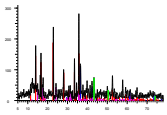	–	+	–	+	–	+
M-B-3	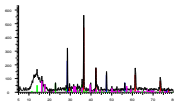	–	+	+	–	–	+
M-B-4	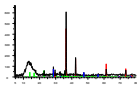	–	+	+	–	–	+
M-B-5	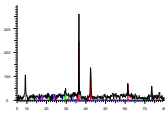	–	+	–	+	–	+
M-B-6	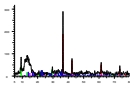	–	+	–	+	–	+
M-B-7	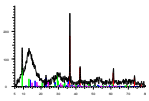	–	+	–	+	–	+

Collectively, the results of these investigations provide a comprehensive picture of metallurgical technology at Qalaichi, demonstrating both the advanced metallurgical skills of its craftsmen in working with different alloys and the methodological differences, analytical limitations, and data variations among the individual studies.

Iron Metallurgy at Qalaichi: Previous investigations indicate that ironworking at Qalaichi had reached a remarkably advanced technological level. Bahadari's study of six iron artifacts using SEM–EDS demonstrated that these objects were manufactured primarily from wrought iron containing very high iron contents (99.3–99.8 wt.%) with only minor amounts of carbon. Trace concentrations of silicon, phosphorus, sulfur, nickel, antimony, and chlorine were also detected, indicating the production of relatively pure iron with limited impurities. In contrast, Soudagar employed ICP–MS to analyze several iron artifacts and reported slightly different iron concentrations ranging from 99.71 to 99.84 wt.%. Similar trace elements, including silicon, phosphorus, sulfur, and chlorine, were identified; however, titanium and variable amounts of antimony were also detected. Although these findings are broadly consistent with those reported by Bahadari, they reveal differences in the concentrations of minor and trace elements, which may reflect variations in raw material sources, smelting practices, or analytical methodology. Although the primary focus of the present study is bronze metallurgy, the corrosion data obtained from both bronze and associated iron artifacts suggest that the occurrence of sulfur- and chlorine-bearing compounds is related not only to the original alloy composition but also to burial conditions and, potentially, to different stages of the ancient metallurgical production sequence.

Bronze Metallurgy at Qalaichi: Soudagar investigated a diverse assemblage of bronze artifacts, including horse harness fittings, bracelets, bronze plaques, decorative studs, and rods. Chemical analyses showed that most objects consisted of copper (91–98 wt.%) and tin (4–15 wt.%), together with minor impurities such as lead, arsenic, antimony, and nickel. Manufacturing techniques included both casting and hammering, while intergranular corrosion, surface deterioration, and green corrosion products, principally malachite and copper chlorides, were identified. The present study employed SEM–EDS to examine seven bronze artifacts and demonstrated that all were manufactured from tin bronze, containing approximately 79–96 wt.% copper and 4–22 wt.% tin. Several specimens contain copper sulfide inclusions, indicating that the smelting process was incomplete and that portions of the original sulfide ore were not fully reduced to metallic copper. Furthermore, many samples exhibit clear evidence of selective corrosion, characterized by copper dissolution (decuprification) accompanied by secondary tin enrichment, a corrosion mechanism widely recognized in archaeological bronze alloys. Taken together, the results of the present investigation and previous studies

indicate that bronze metallurgy at Qalaichi relied primarily on copper–tin alloys with variable tin contents, produced through a combination of casting and mechanical working techniques. The artifacts subsequently experienced complex post-depositional alteration processes, including selective corrosion and mineral transformation. These findings contribute to a more comprehensive understanding of both the metallurgical technology employed at Qalaichi and the long-term burial-induced changes affecting its archaeological bronze assemblage.

Corrosion and Deterioration: The results of previous investigations provide complementary insights into the post-burial deterioration processes affecting the metallic artifacts from Qalaichi. Although Bahadari's study did not specifically focus on corrosion mechanisms, the detection of trace amounts of chlorine and sulfur in several iron samples suggests that corrosive processes had occurred during burial. Soudagar documented green surface corrosion products, including malachite, atacamite, and copper chlorides, together with intergranular corrosion in numerous bronze artifacts. In addition, adhering soil deposits

Table 3: Comparative summary of previous and present studies on the metallurgy of the Qalaichi archaeological site (Authors, 2025). ▼

Research Aspect	Bahadari (Iron Artifacts)	Soudagar (Bronze and Iron Artifacts)	Present Study (Bronze Artifacts)
Iron metallurgy	High-purity wrought iron (99.0–99.8 wt.% Fe) with low carbon content; minor impurities including Si, P, S, Ni, Sb, and Cl.	High-purity iron (99.71–99.84 wt.% Fe) containing relatively higher levels of Cl, Cu, S, Ni, P, and Sb.	Limited direct evidence; indirect indications of sulfur- and chlorine-bearing compounds associated with corrosion and burial conditions.
Bronze metallurgy	Not investigated.	Bronze alloys containing 91–98 wt.% Cu and 4–15 wt.% Sn, with minor Sb, Pb, As, and Ni; manufacturing techniques included casting and hammering.	Tin bronze alloys containing 79–96 wt.% Cu and 4–22 wt.% Sn; presence of copper sulfide inclusions; evidence of selective corrosion (decuprification) and secondary tin enrichment.
Corrosion and deterioration	Indirect evidence of corrosion is inferred from trace amounts of chlorine and sulfur.	Green surface corrosion products, dark patina, and intergranular corrosion were observed.	Selective corrosion, microcracks, selective copper dissolution (decuprification), and copper sulfide inclusions identified through microstructural and SEM–EDS analyses.
Technological significance	Demonstrates advanced production of high-purity wrought iron.	Indicates a diverse bronze industry employing multiple manufacturing techniques.	Provides a more detailed understanding of metallurgical processes, including incomplete smelting, preservation of sulfide inclusions, and post-depositional corrosion mechanisms.

and dark patina layers were observed on several objects, indicating prolonged interaction with the burial environment. The present study, based on microstructural examination, SEM–EDS analysis, and XRD characterization, identified clear evidence of selective corrosion (decuprification), strain lines, microcracks, and copper sulfide inclusions preserved within the metallic matrix. The marked depletion of copper accompanied by the relative enrichment of tin in the corroded regions further confirms the occurrence of selective corrosion, demonstrating that the post-depositional alteration of these artifacts was largely governed by both the original alloy composition and the physicochemical conditions of the burial environment. Overall, the combined results of these studies indicate that the archaeological metals from Qalaichi underwent complex corrosion processes involving oxidation, chloride-induced degradation, and selective dissolution of copper, while preserving valuable metallurgical information regarding ancient manufacturing technology and the long-term effects of burial.

The synthesis of the three independent investigations demonstrates that metallurgical production at Qalaichi attained a notably high degree of technological sophistication in both ferrous metallurgy and copper-alloy production. Bahadari's research highlights the high quality of wrought-iron manufacture, indicating effective bloom refining and the production of relatively pure iron containing minimal impurities. Soudagar's study reveals the compositional diversity of bronze alloys and the application of multiple manufacturing techniques, including casting and mechanical working. Building on these earlier studies, the present investigation provides a more detailed reconstruction of ancient metallurgical practices through integrated SEM–EDS, metallographic, and XRD analyses, elucidating both alloy-production technology and the physicochemical processes responsible for post-depositional alteration. The results further demonstrate that the bronze artifacts were manufactured from tin-bronze alloys with variable tin contents and preserve microstructural evidence of incomplete smelting, including unreduced copper sulfide inclusions. In addition, characteristic corrosion phenomena, such as selective copper dissolution (decuprification), secondary tin enrichment, intergranular corrosion, and the formation of stable and metastable corrosion products, provide valuable information on the long-term interaction between alloy composition and the burial environment. These observations not only contribute to the reconstruction of ancient metallurgical practices but also enhance our

understanding of the diagenetic evolution of archaeological copper alloys. Despite the overall consistency among the three studies, several discrepancies remain, particularly concerning the concentrations of minor and trace elements and the interpretation of corrosion intensity and alteration mechanisms. Such differences may reflect variations in analytical methodology, sampling strategy, object selection, or intrinsic heterogeneity within the alloys themselves.

Consequently, a comprehensive reconstruction of metallurgical technology at Qalaichi requires further interdisciplinary research integrating archaeometallurgical, metallographic, mineralogical, and geochemical datasets. Taken together, these investigations constitute the most comprehensive assessment currently available of metallurgical technology at Qalaichi. Bahadari's work establishes the advanced technological level of wrought-iron production; Soudagar documents the compositional variability and manufacturing techniques of both iron and bronze artifacts; and the present study substantially expands current knowledge by providing detailed evidence concerning alloy microstructures, smelting efficiency, manufacturing technology, corrosion mechanisms, and post-depositional transformation processes. Collectively, these findings demonstrate that metallurgical production at Qalaichi was technologically sophisticated in both the manufacture of high-purity wrought iron and the production of tin-bronze alloys. Nevertheless, the observed inconsistencies in impurity distributions and corrosion characteristics indicate that further comparative investigations employing high-resolution analytical techniques, integrated with quantitative metallography and broader archaeometric approaches, are necessary to achieve a more definitive reconstruction of metallurgical production and technological practices at this important Iron Age center.

Conclusion

The archaeometallurgical and microstructural investigation of the metal artifacts recovered from the Qalaichi archaeological site provides a comprehensive assessment of metalworking technologies employed during the Mannaean period. The assemblage is dominated by tin-bronze alloys with variable tin contents, indicating that ancient metalworkers intentionally controlled alloy composition to optimize casting properties, mechanical performance, and long-term durability. Only two artifacts were identified as essentially pure copper, whereas the

remaining objects were manufactured from tin bronze. Such deliberate alloy selection reflects a sophisticated understanding of the relationship between alloy composition and the mechanical properties of copper alloys. Sample M-A-1 preserves clear evidence of a manufacturing sequence involving repeated cycles of cold working followed by annealing, ultimately producing a highly workable microstructure. This technological strategy combined strain hardening with recrystallization, thereby restoring ductility while maintaining adequate mechanical strength, and indicates an advanced knowledge of the thermal behaviour of copper alloys. Sample M-A-4, also manufactured from tin bronze, exhibits evidence of limited heat treatment together with moderate surface corrosion. Sample M-B-1 is characterized by intergranular cracking and corrosion accompanied by significant copper depletion and relative tin enrichment.

These features are consistent with selective phase corrosion, in which the copper-rich phase dissolved preferentially relative to the tin-rich phase. The occurrence of elongated inclusions and preserved strain lines further indicates repeated cycles of mechanical deformation and annealing, with a final annealing stage likely undertaken to reduce brittleness induced by extensive cold working. Sample M-B-3 exhibits an exceptionally fine-grained microstructure together with bent and fragmented annealing twins, indicating intensive mechanical deformation during the final stages of manufacture. Among the investigated artifacts, this specimen preserves the most complex thermomechanical history. The elongated sulfide inclusions observed within the metallic matrix likewise attest to prolonged mechanical working following casting. In sample M-B-4, although mechanical working was applied during the final stage of manufacture, the degree of microstructural deformation is relatively limited. This observation may indicate either a final stress-relief annealing treatment or comparatively mild cold working. These features suggest deliberate control of the balance between hardness and ductility during artifact production. Sample M-B-5 represents one of the most severely deteriorated artifacts in the assemblage. Manufactured from tin bronze, it exhibits extensive selective corrosion (decuprification), whereby preferential dissolution of the copper-rich phase has produced a highly porous and exfoliated microstructure. The advanced degradation has effectively produced a naturally etched microstructure, exposing internal metallographic features through corrosion. Similarly, sample M-B-6 displays advanced

corrosion associated with abundant copper sulfide inclusions. These inclusions most likely originated from incompletely reduced sulfide ores during smelting and subsequently acted as preferential sites for corrosion propagation.

Their presence, combined with extensive corrosion, contributed to severe microstructural degradation and the development of heterogeneous, mechanically weakened regions. Although sample M-B-7 was likewise manufactured from tin bronze, prolonged corrosion has extensively altered its original microstructure, obscuring many of the primary metallurgical features and complicat ing the interpretation of its manufacturing history. The X-ray diffraction (XRD) analyses further confirmed the presence of a diverse assemblage of corrosion minerals, including cuprite (Cu_2O), brochantite ($Cu_4SO_4(OH)_6$), nantokite (CuCl), malachite ($Cu_2CO_3(OH)_2$), and gypsum ($CaSO_4 \cdot 2H_2O$). These mineral assemblages reflect varying burial environments and corrosion pathways. The identification of nantokite indicates the involvement of chloride ions and suggests that at least some artifacts were subjected to chloride-induced corrosion associated with moist or saline burial conditions, potentially increasing their susceptibility to bronze disease. Overall, the archaeometallurgical and corrosion analyses demonstrate that Mannaean metalworkers possessed sophisticated knowledge of alloy production and thermomechanical processing. The intentional adjustment of alloy composition, repeated cycles of cold working and annealing, careful control of manufacturing temperatures, and selection of appropriate copper–tin alloy compositions collectively reflect a highly developed technological tradition. These practices reveal not only an advanced understanding of the mechanical behaviour of copper alloys but also considerable technical skill in the production of functional and durable metal artifacts. Furthermore, the integrated application of metallography, SEM–EDS, and XRD has enabled the reconstruction of both the original manufacturing technology and the long-term post-depositional alteration processes affecting these archaeological metals, thereby contributing to a more comprehensive understanding of Iron Age metallurgy in northwestern Iran.

Acknowledgments

The authors extend their sincere gratitude to the anonymous peer reviewers for their insightful critiques and constructive suggestions,

which significantly enhanced the clarity and scholarly rigor of this manuscript.

Observation Contribution

The contribution of all authors to the writing of the article has been equal.

Conflict of Interest

The Authors, while observing publication ethics in referencing, declare the absence of conflict of interest.

References

- Bahadari, R., (1998). Barrasi-ye khordegi-ye ashya-ye ahani va motale'e-ye chand shay'-e ahani makshufeh az kavosh-e Bukan. In R. Vatandoost (Ed.), *Proceedings of the Research Institute for Conservation and Restoration of Historical and Cultural Objects* (Vol. 1, pp. 46–51). Research Institute for Conservation and Restoration of Historical and Cultural Objects, Iranian Cultural Heritage Organization. (In Persian).

- Bahadari, R. & Ahmadi, S. H. (2000). Barrasi-ye khordegi-ye ashya-ye ahani kashf shodeh az hafari-ye Bukan. *Iranian Journal of Crystallography and Mineralogy,* 8(2): 117–125. (In Persian).

- Bakhshandehfard, H. (2010). *Barrasi-ye athar-e tarikhi-ye felezi dar marammat.* Isfahan University of Art Press. (In Persian).

- Behzadi, R. (1993). Gowm-ha-ye kam shenakhteh-ye kohan: Manaha. *Chista*, 89–90: 1043–1060. (In Persian).

- Craddock, P. T. (1995). Early metal mining and production. Smithsonian Institution Press.

- Dyson, R. H., Jr. (1965). Problems of protohistoric Iran as seen from Hasanlu. *Journal of Near Eastern Studies,* 24(3): 193–217. https://doi.org/10.1086/371815

- Frahm, E. (2014). Scanning electron microscopy (SEM): Applications in archaeology. In C. Smith (Ed.), *Encyclopedia of global archaeology. Springer.* https://doi.org/10.1007/978-1-4419-0465-2_341

- Hassanzadeh, Y. (2006). Tahlil-e amari-ye baghayaye memari-ye mahvouteh-ye Mannayi-ye Qalaichi, Bukan. *Archaeological Research and Interdisciplinary Studies,* 3(9): 48–56. (In Persian).

- Hassanzadeh, Y. (2022). An archaeological view to the Mannaean Kingdom. *AsiAnA: Asia Anteriore Antica: Journal of Ancient Near Eastern Cultures,* 4: 13–46. https://doi.org/10.36253/asiana-1746

- Kargar, B. (2004). Qalaichi: Izirtu, a Mannaean centre of Period

IB. In M. Azarnoush (Ed.), *Proceedings of the International Conference on Iranian Archaeology: Northwestern Iran* (pp. 229–245). Research Institute of Archaeology, Iranian Cultural Heritage Organization. (In Persian).

- Malekzadeh, M. (2009). Padshahi-ye Mana, dowreh-ye Mad va tarikh-e Iran-e bastan. *Bastanpazhuhi*, 7: 41–44. (In Persian).

- Molazadeh, K. (2009). Padshahi-ye Mana: Negahi be sakhtarhaye farhangi, ejtemaei va siyasi-ye Mana bar asas-e danesh-e bastan-shenasi va joghrafia-ye tarikhi. *Bastanpazhuhi*, 7: 45–53. (In Persian).

- Muscarella, O. W. (1988). *Bronze and iron: Ancient Near Eastern artifacts in the Metropolitan Museum of Art.* Metropolitan Museum of Art.

- Oudbashi, O. & Davami, P. (2014). Metallography and microstructure interpretation of some archaeological tin bronze vessels from Iran. *Materials Characterization,* 97: 74–82. https://doi.org/10.1016/j.matchar.2014.09.007

- Qodratabadi, S. & Hassanzadeh, Y. (2009). Qaplantu: Mahvouteh-i kam shenakhteh dar markaz-e sarzamin-e Mana. *Bastanpazhuhi*, 7: 93–99. (In Persian).

- Robbiola, L., Blengino, J. M. & Fiaud, C. (1998). Morphology and mechanisms of formation of natural patinas on archaeological Cu–Sn alloys. *Corrosion Science,* 40(12): 2083–2111. https://doi.org/10.1016/S0010-938X(98)00096-1

- Rostoker, W., Pigott, V. C. & Dvorak, J. (1989). Direct reduction to copper metal by oxide–sulphide mineral interaction. *Archaeomaterials*, 3: 69–87.

- Scott, D. A. (1991). *Metallography and microstructure of ancient and historic metals.* Getty Conservation Institute.

- Scott, D. A. (2002). *Copper and bronze in art: Corrosion, colorants, conservation*. Getty Conservation Institute.

- Selwyn, L. S. (2006). Corrosion of metal artifacts in buried environments. In: *ASM handbook: Corrosion: Environments and industries* (Vol. 13C, pp. 306–322). ASM International. https://doi.org/10.31399/asm.hb.v13c.a0004142

- Soudagar, L. (1995). “Shenasaei va motale’e-ye fanni-ye athar-e felezi be dast amadeh az hafari-ye mantaghe-ye Bukan”. Master’s thesis, Isfahan University of Art. (In Persian).

- Stewart, B. (2007). *Analytical techniques in materials conservation*. John Wiley & Sons.

- Yaghmaei, E. (2023). *Tasir-e farhang-e Ashuri bar Mannaian: Bar payeh-ye kavosh-haye bastan-shenasi dar Tapeh-ye Qalaichi, Bukan*. Dadkin Publications. (In Persian).

فصلنامهٔ علمی پژوهش‌های باستان‌شناسی ایران
P. ISSN: 2345-5225 & E. ISSN: 2345-5500
نشانی پایگاه نشریه: https://nbsh.basu.ac.ir
شمارهٔ ۴۹، دورهٔ شانزدهم، ۱۴۰۵
انجمن علمی باستان‌شناسی ایران
دانشگاه بوعلی سینا

فناوری ساخت و مکانیسم‌های خوردگی آثار فلزی باستانی تپه قلایچی

حمیدرضا بخشنده‌فرد[I]، زهرا رحیمی‌کلیشادی[II]، فرشید ایروانی‌قدیم[III]

شناسهٔ دیجیتال (DOI): https://doi.org/10.22084/nb.2025.9515.2664
تاریخ دریافت: ۱۴۰۳/۰۱/۱۷، تاریخ بازنگری: ۱۴۰۳/۰۴/۲۶، تاریخ پذیرش: ۱۴۰۳/۰۵/۰۷
نوع مقاله: پژوهشی
صص: ۱۸۱-۱۴۷

چکیده

مانناییِ اقوامی بودند که در هزارهٔ اول پیش‌ازمیلاد در نواحی شمال‌غرب ایران زندگی می‌کردند. محوطهٔ قلایچی براساس کشفیات انجام‌شده از محوطه‌های مانناییِ در قرن هشتم و هفتم پیش‌ازمیلاد است. در این محوطه کاوش‌های غیرمجاز بسیاری صورت گرفته بود و پس از آن کاوش‌های روشمند توسط «اسماعیل یغمایی» و «بهمن کارگر» در این منطقه صورت گرفت. تعداد ۹ قطعهٔ فلزی حاصل از این محوطه طی کاوش‌های سال‌های ۱۳۸۱ تا ۱۳۸۳هـ.ش. به سرپرستی بهمن کارگر مربوط به هزارهٔ اول پیش‌ازمیلاد برای مطالعه انتخاب شده است که شامل دو گروه است؛ در گروه اول، یک دستبند و یک تکه شئ فلزی و در گروه دوم نیز هفت تکه شئ فلزی وجود دارد. هدف این پژوهش شناسایی دقیق آن‌ها از نظر ساختاری و فن‌شناسی و چگونگی ساخت و شناخت نوع و فرآیند خوردگی و محصولات خوردگی آن‌ها است. این یافته‌ها، باتوجه به موقعیت جغرافیایی و دورهٔ زمانی (هزارهٔ اول پیش‌ازمیلاد)، اهمیت فراوانی در بازسازی روندهای تکنولوژی، فرهنگی و اجتماعی جوامع عصر آهن در منطقه دارند. پرسش پژوهش شامل: ۱) روش ساخت از نظر ساختار و ساختمان چیست؟ ۲) محصولات خوردگی در این نمونه‌ها چیست و پایداری آن‌ها چگونه است؟ ۳) روند خوردگی و فرآیند اثرگذار محیطی بر این آثار چگونه است؟ به این‌منظور بررسی‌های میکروسکوپی و آنالیز دستگاهی XRD، SEM-EDX و متالوگرافی انجام شد. مطالعات ریزساختاری و SEM-EDX نشان‌داد، کار سرد، گرم و تابکاری بر روی نمونه‌ها انجام شده است. نتایج به‌دست‌آمده از آنالیز XRD فازهای خوردگی نمونه‌ها شامل: مالاکیت، نانتوکیت، کوپریت، بروکانتیت و پیپایت شناسایی شد. برای این‌منظور از بررسی‌های میکروسکوپی و آنالیز تکنیک ابزاری SEM-EDX و متالوگرافی استفاده شد. نتایج آزمایش‌ها نشان‌داد که تمام قطعات اشیاء به جز دو نمونه از آلیاژ مفرغ و دو نمونه از مس ساخته شده‌اند. به‌طورکلی می‌توان گفت مطالعات SEM-EDX انجام‌شده در بررسی ساختار و نحوهٔ ساخت نمونه‌ها نشان‌دهندهٔ شباهت آن‌هاست.

کلیدواژگان: تپه قلایچی، فرهنگ مانناییِ، فناوری ساخت، سازوکارهای خوردگی، SEM–EDS.

I. گروه حفاظت و مرمت، دانشکدهٔ مرمت دانشگاه هنر اصفهان، اصفهان، ایران (نویسندهٔ مسئول).
Email: hr.bakhshan@aui.ac.ir
II. گروه حفاظت و مرمت، دانشکدهٔ مرمت دانشگاه هنر اصفهان، اصفهان، ایران.
III. گروه باستان‌شناسی ، دانشکدهٔ حفاظت آثار، دانشگاه هنر اسلامی تبریز، آذربایجان شرقی، تبریز، ایران.

ارجاع به مقاله: بخشنده‌فرد، حمیدرضا؛ رحیمی‌کلیشادی، زهرا؛ و ایروانی‌قدیم، فرشید، (۱۴۰۵). «فناوری ساخت و مکانیسم‌های خوردگی آثار فلزی باستانی تپه قلایچی». پژوهش‌های باستان‌شناسی ایران، ۱۶(۴۹): ۱۴۷-۱۸۱. https://doi.org/10.22084/nb.2025.9515.2664

فصلنامهٔ علمی گروه باستان‌شناسی دانشکدهٔ هنر و معماری، دانشگاه بوعلی‌سینا، همدان، ایران.

حق انتشار این مستند، متعلق به نویسنده(گان) آن است. ۱۴۰۵ © ناشر این مقاله، دانشگاه بوعلی‌سینا است. این مقاله تحت گواهی زیر منتشرشده و هر نوع استفاده غیرتجاری از آن مشروط بر استناد صحیح به مقاله و با رعایت شرایط مندرج در آدرس زیر مجاز است.
Creative Commons Attribution-NonCommercial 4.0 International license (https://creativecommons.org/licenses/by-nc/4.0/).
© The Author(s)
OPEN ACCESS